CHEMISTRY OF MATERIALS

pubs.acs.org/cm Article

Iron-Content-Dependent, Quasi-Static Dielectric Resonances and Oxidative Transitions in Bornite and Chalcopyrite Copper Iron Sulfide Nanocrystals

Soohyung Lee,[#] Sandeep Ghosh,[#] Chad E. Hoyer, Hongbin Liu, Xiaosong Li, and Vincent C. Holmberg*

Cite This: *Chem. Mater.* 2021, 33, 1821−1831 Read Online

ACCESS | Metrics & More | Article Recommendations | Supporting Information

ABSTRACT: Manipulation of material composition can often induce unprecedented optoelectronic changes in semiconductor nanocrystals (NCs). Here, we demonstrate that bornite-phase copper iron sulfide (Cu_5FeS_4) NCs exhibit tunable optical characteristics from visible to near-infrared (NIR) that are strongly dependent on their iron content. These stoichiometry-dependent optical modulations confirm that the origin of the spectral response in these NCs is due to the occurrence of two fundamentally different types of resonant excitation: (i) a quasi-static dielectric resonance (DR) and (ii) a localized surface plasmon resonance (LSPR). Electronic band structure calculations by density functional theory (DFT) show that the presence of an intermediate band (IB) of states formed by empty Fe d-orbitals gives rise to the occurrence of a DR in the visible-frequency regime, analogous to the observed optical response in all-dielectric IB chalcopyrite ($CuFeS_2$) NCs. Moreover, as the Fe content of the NCs is decreased *via* aerobic oxidation, the intensity of the DR diminishes, accompanied by a concomitant rise in the intensity of a hole-induced LSPR response in the NIR, reminiscent of self-doped copper sulfide NCs. Notably, the spectral position of the DR does not change as its intensity is reduced, clearly differentiating this mode of resonant excitation from the well-known LSPR response, which shifts substantially in frequency as the free-carrier concentration is modified. We further demonstrate an analogous DR-to-LSPR evolution in $CuFeS_2$ NCs subjected to the influence of oxidizing agents and added ions. The decreased Fe content significantly reduces the contributions of Fe 3d orbitals to the IB in these ternary Cu−Fe−S NCs, resulting in a reduced DR intensity, and as the composition approaches a more Cu−S-like system, the vacancy-induced LSPR intensity becomes more pronounced. This is an example of compositionally induced DR-to-LSPR optical modulation in colloidal nanomaterials, which could be useful in dynamically responsive material applications and as a synthetic strategy for engineering desired spectral responses in semiconductor NCs.

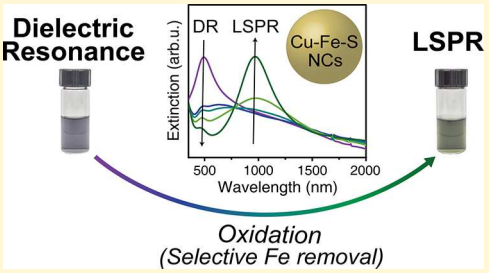

INTRODUCTION

Transition metals with partially filled d-orbitals are known to bestow interesting electronic, magnetic, and optical characteristics to the materials they constitute.[1−5] For instance, Re^{6+} being a d^1 system confers metallic character to rhenium (+6) oxide,[3,6] while the incorporation of Cr^{3+} (d^1 system) enables lower-energy photon absorption in relatively wide band gap semiconductors like $CuGaS_2$.[7] In metal sulfides, this influence manifests in the form of delocalized d-levels, which form a narrow band near the top of the valence band (VB) or deep in the band gap.[5,8,9] The presence of this intermediate band (IB) has been demonstrated to render hitherto unknown optical responses at the nanoscale, as has recently been demonstrated for colloidal nanocrystals (NCs) of $CuFeS_2$[5,10,11] and Cu_3VS_4.[4,12,13] Further, from the perspective of practical applications, IB semiconductor NCs are of significance as they enable a more efficient absorption of solar radiation,[14,15] improved thermoelectric efficiency,[16,17] and can be used as photothermal agents for cancer therapy.[5,18−20]

Among the nanoscale metal chalcogenides, colloidal NCs of copper chalcogenides have been actively studied in recent times, owing to their structural, compositional, and stoichiometric versatility, and more importantly, for the "self-doped" intrinsic formation of copper vacancies that lead to the localized surface plasmon resonance (LSPR) response in the near-infrared (NIR) region of the electromagnetic spectrum.[21−25] This optical response of binary copper chalcogenide NCs is tunable through manipulation of their composition, and the same principles have lately been extended to ternary and quaternary chalcogenide NCs as well,[25−27] albeit the mechanism underlying the optical responses can be fundamentally different in different material systems. For instance, in contrast to the widely studied plasmonic Cu−S NCs, Ghosh and Gaspari et al. recently showed that a metal-like optical response in chalcopyrite $CuFeS_2$ NCs can be attributed to its

Received: December 16, 2020
Revised: February 15, 2021
Published: February 26, 2021

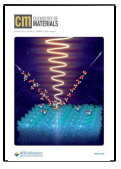

https://dx.doi.org/10.1021/acs.chemmater.0c04798
Chem. Mater. 2021, 33, 1821−1831

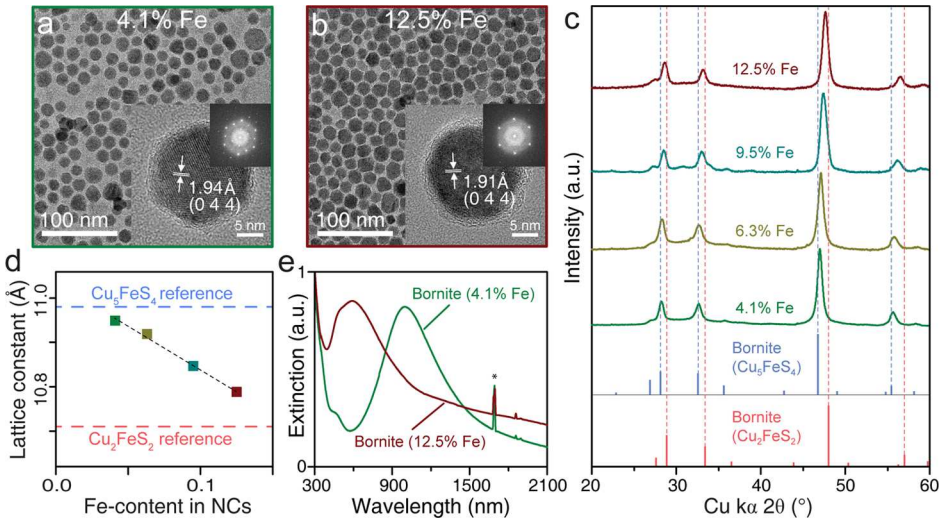

Figure 1. Structural and morphological characterization of the as-synthesized bornite NCs. The TEM images of (a) low-Fe and (b) high-Fe bornite NCs; insets show the respective HRTEM images and fast Fourier transforms of individual NCs. (c) XRD patterns of NC samples with varied Fe content, in comparison to reference lines for bornite Cu_5FeS_4 (PDF #98-000-6587; blue lines) and bornite Cu_2FeS_2 (PDF #98-000-4849; red lines). (d) Bornite NC lattice constants determined from the XRD patterns in panel c, flanked by representative bornite polymorphs. (e) UV−vis−NIR extinction spectra of as-synthesized bornite NCs with the lowest and highest Fe content. Spectral artifacts caused by the NIR absorption bands of the chloroform solvent are marked by asterisks.

unique band structure, which constitutes an IB of states generated by empty Fe 3d orbitals.[5,10] Remarkably, when the IB is sufficiently close to the VB edge, the material can exhibit a negative real permittivity across a broad range of visible frequencies.[10] This negative real permittivity enables a Fröhlich resonance condition, leading to a quasi-static dielectric resonance (DR) and associated resonant absorption in the visible-frequency regime, despite a complete lack of ground-state free charge carriers, as demonstrated in nanoscale $CuFeS_2$.[5,10]

The presence of Fe, as the transition metal with partially filled d-orbitals, is then the defining factor in the optical signatures from these Cu−Fe−S systems. Similar to the experiments on binary Cu−S NCs, a modulation of this optical response through changing compositions has been demonstrated in some nanoscale Cu−Fe−S semiconductors.[28−30] For instance, the introduction of Cd in Cu−Fe−S NCs rendered them luminescent,[28] while a modulation of the DR was demonstrated through changing the S:Se ratio in $CuFeS_{2-x}Se_x$ alloyed NCs.[30] However, a comprehensive demonstration of the influence of changing Fe content on the optical responses of Cu−Fe−S NCs is necessary to develop a proper understanding of the spectral influence of the Fe 3d orbitals and devise practical applications of these nanoscale semiconductors.

Here, we investigate the influence of iron content on the optical resonances and, concomitantly, the electronic structure of bornite-phase, copper iron sulfide NCs, synthesized *via* a colloidal hot-injection route. The synthesis entails rapidly introducing a reactive sulfur precursor into a hot solution of copper and iron precursors in admixture with excess halide ions and organic surfactants. This halide-assisted synthetic method enabled both a monodisperse size distribution and control over the composition of the as-synthesized bornite NCs, allowing for delineation of the relationship between Fe content, electronic structure, and the spectral characteristics of nanoscale Cu−Fe−S systems. As the Fe content of the as-synthesized bornite NCs was varied from 4.1 to 12.5%, significant changes in their optical extinction spectra were observed, with high-Fe-content NCs exhibiting the appearance of a strong absorption band in the visible-frequency regime (centered at 490 nm; 2.53 eV), which we attribute to a Fe 3d IB-associated DR, while the low-Fe-content NCs exhibit an NIR LSPR response (centered at 1000 nm; 1.24 eV). Further, a DR-to-LSPR transition could be induced *via* simple aerobic oxidation of the as-synthesized bornite NCs, which was ascribed to the oxidatively driven removal of Fe (out of the NCs) by careful elemental analysis of the NC composition. A similar spectral transition was also demonstrated on chalcopyrite ($CuFeS_2$) NCs *via* controlled oxidation and addition of ions, which further corroborates the role of Fe 3d orbitals in the emergence of the visible-frequency DR centered at 490 nm (2.53 eV) in nanoscale Cu−Fe−S systems. Density functional theory (DFT) calculations lend additional evidence in this regard, showing an increased contribution to the density of states (DOS) in the IB as the Fe content of the bornite NCs is increased. These spectral changes are visually discernible, as the DR induces a purple-colored NC dispersion while the LSPR leads to a green color, for both bornite and chalcopyrite NCs. These joint investigations validate that the intense 490 nm band in nanoscale Cu−Fe−S systems cannot be attributed to the more widely known LSPR response that arises from the collective oscillations of free charge carriers and is indeed due to their unique band structure that contains an intermediate Fe d-band that enables a Frölich resonance in the visible region. These optical modulations *via* compositional tuning yield a more holistic understanding of the DR response of Cu−Fe−S NCs and can be further engineered into dynamic material systems.

RESULTS AND DISCUSSION

The synthesis of bornite-phase copper iron sulfide NCs with controlled iron content was performed *via* hot injection on a Schlenk line, where a reactive sulfur precursor (hexamethyldisilathiane in octadecene) was rapidly injected into a hot solution of copper(II) and iron(III) chlorides in a mixture of

https://dx.doi.org/10.1021/acs.chemmater.0c04798
Chem. Mater. 2021, 33, 1821−1831

trioctylphosphine oxide, oleylamine, oleic acid, and octadecene. The metal−precursor solution was also charged with excess sodium chloride, to ensure that the reaction medium was halide rich. The presence of excess halide species was necessary to obtain the desired iron content while maintaining a monodisperse size distribution in these NCs,[31] as it is important to balance the reactivity of the two metal precursors for a chosen stoichiometry in ternary copper chalcogenide NCs,[5,32] as has been demonstrated previously for various colloidal NCs.[32−34] When the synthesis was performed with no added halide ions in the system, large, polydisperse, low-iron-content bornite NCs with a platelet-like morphology resulted, predominantly exhibiting a broad NIR LSPR optical signature (Figure S1). However, for the experiments described herein, it was critical that samples of monodisperse, phase-pure bornite NCs with tunable iron content were produced (Figure S2), both of which were achieved *via* the presence of the excess halide ions. In these syntheses, the quantity of $FeCl_3$ was adjusted relative to a fixed amount of $CuCl_2$, with representative transmission electron microscopy (TEM) and high-resolution TEM (HRTEM) images of the resulting NCs shown in Figure 1. Iron contents ranging from 4.1 atomic % (Figure 1a) to 12.5 atomic % (Figure 1b) were obtained, as determined by elemental analysis *via* energy-dispersive X-ray spectroscopy (EDXS) (Table S1), and these stoichiometries are, respectively, referred to as "low-Fe" and "high-Fe" bornite in this work. As a reference, the crystal structure of the two major bornite polymorphs, Cu_5FeS_4 (10 atomic % Fe) and Cu_2FeS_2 (20 atomic % Fe), is shown in Figure S3, where S atoms form a face-centered cubic lattice with Cu and Fe atoms residing in a subset of the tetrahedral sites, as compared to the fully tetragonal chalcopyrite $CuFeS_2$ structure. The iron-content difference between these bornite polymorphs can be appreciated from the fact that in a unit cell, a Cu atom in Cu_5FeS_4 is essentially replaced by an Fe atom in Cu_2FeS_2 (or $Cu_4Fe_2S_4$, for the sake of clarity), and considering that the NCs reported here exhibit stoichiometries which can be interpolated between these extreme cases, this system is particularly well suited for studying the effect of Fe content on the optical signatures exhibited by nanoscale Cu−Fe−S materials. In comparison, the main difference between the bornite and chalcopyrite structures is in the relative occupation of tetrahedrally coordinated Cu and Fe atoms, as can be appreciated from their crystal structures shown in Figure S3.

The tighter size control afforded by the halide-assisted synthesis can be discerned from the fact that the as-synthesized NCs exhibit a relatively uniform size distribution with average diameters of 16.2 ± 2.1 and 15.4 ± 1.4 nm, respectively, for the low-Fe and high-Fe compositions (Figure S2). HRTEM images (insets, Figure 1a,b) reveal the single-crystalline nature of the as-synthesized NCs, with the measured interplanar distances corresponding to the (044) lattice planes of the cubic bornite structure. Interestingly, the measured interplanar spacing was found to be dependent on the Fe content of the NCs, with higher Fe-content NCs exhibiting a narrower (044) d-spacing. This is suggestive of lattice compression as the Fe content in the NC increases, and indeed this can be correlated with the smaller ionic radius of Fe (compared to Cu), leading to a decreased lattice constant as the Fe atoms progressively replace Cu atoms in the NC lattice. In fact, a more general set of evidence in this regard is obtained from X-ray diffraction (XRD) measurements (Figure 1c), which further corroborates the observed trend. The high-Fe bornite NC diffraction patterns can be clearly ascribed to the cubic bornite phase (Figure 1c), with the indexed diffraction peaks systematically shifting toward higher Bragg angles upon increasing Fe content. As mentioned above, the NCs reported herein exhibit stoichiometries that range between the bornite polymorphs of Cu_5FeS_4 and Cu_2FeS_2, and this fact is also apparent in the XRD patterns shown in Figure 1c. Cu_2FeS_2 exhibits higher Bragg angles in comparison to Cu_5FeS_4, in line with the fact that Cu_2FeS_2 has a higher Fe content (20%) and the high-Fe bornite NCs (12.5% Fe) actually exhibit Bragg angles closer to the Cu_2FeS_2 polymorph. On the other hand, low-Fe bornite NCs (4.1% Fe) have Bragg angles closer to the Cu_5FeS_4 polymorph, while the other stoichiometries systematically fall in between these cases. In addition, this systematic shift in the XRD patterns confirms that the additional iron has been uniformly incorporated into the crystal lattice.[35,36] The lattice constants calculated from each of the measured XRD patterns are plotted in Figure 1d as a function of the measured Fe content for each respective sample. Notably, the calculated lattice constants are remarkably consistent with the lattice parameters determined from TEM (Figure S4), with the results of both measurements shown overlaid in Figure S5. However, the most striking difference between the low-Fe and high-Fe bornite NCs is in their optical extinction profiles (Figure 1e), which were found to exhibit strong, resonant extinction features with iron-content-dependent intensities at distinct visible and NIR frequencies. As discussed in detail below, we attribute these extinction features to two fundamentally different types of resonant excitation.

Since the absorption and scattering cross-sections of a colloidal nanostructure are directly related to its polarizability, where $\sigma_{abs} = k\cdot\mathrm{Im}\{\alpha\}$, $\sigma_{scat} = \frac{k^4}{6\pi}|\alpha|^2$, and k is the wavevector of the incident light, the wavelengths at which resonant extinction features occur can be readily determined *via* an examination of the polarizability, α, of the nanostructure, which can be extracted by solving Maxwell's equations for a dielectric particle subjected to an incident electromagnetic wave.[37] For a nanostructure with a spherical shape, the resulting polarizability is given by the following Mie theory expression

$$\alpha = 3\epsilon_0 V \frac{(\varepsilon - \varepsilon_m)}{(\varepsilon + 2\varepsilon_m)}$$

where ϵ_0 is the permittivity of free space, V is the volume of the nanostructure, ε_m is the dielectric function of the surrounding medium, and ε is the complex permittivity of the nanostructure itself.[37] At certain frequencies, depending on the relative permittivities of the nanostructure and the surrounding medium, the denominator of the above expression for the polarizabilty approaches zero, resulting in a divergent polarizibility and subsequent resonant absorption and scattering profiles.[37] For a dielectric sphere, the Frölich resonance condition (where $\varepsilon + 2\varepsilon_m \rightarrow 0$) occurs at specific frequencies where the real component of the nanostructure permittivity, ε', is equal to $-2\varepsilon_m$.[37] Thus, for colloidal NCs with typical ligands and solvent media, resonant absorption and scattering features occur at frequencies where the real component of the nanostructure dielectric function becomes negative.[3,21,38]

For metallic and highly doped semiconductor nanostructures, it is the high density of free charge carriers that enables a negative real permittivity, typically in the visible-to-infrared frequency regime, resulting in the collective, coherent excitation of a LSPR at the frequency where the polarizability

https://dx.doi.org/10.1021/acs.chemmater.0c04798
Chem. Mater. 2021, 33, 1821−1831

of the structure diverges.[21,38,39] While free-charge-carrier-enabled LSPRs are perhaps the most well-known class of resonant excitation in colloidal nanomaterials, it should be noted that other important modes of resonant excitation also exist. Since the permittivity of an inorganic material is a complex, additive function with many components, including free-carrier contributions, interband and intraband electronic excitations, and phononic vibrational excitations, these collective contributions can give rise to negative real permittivities at a variety of frequencies.[38] For example, many inorganic dielectric materials exhibit high-frequency negative permittivities, and Mie resonances at the corresponding energies in the ultraviolet are quite common.[3,40,41] Moreover, as mentioned earlier in the introduction, it was recently demonstrated that IB semiconductor NCs can exhibit visible-frequency negative real permittivities that give rise to strong, visible-frequency DR if the material possesses an IB of states that lies in close proximity to the edge of the VB.[10]

As can be seen in Figures 1e and S9, low-Fe and high-Fe bornite NCs exhibit dramatically different UV−vis−NIR extinction spectra that depend strongly on the Fe content of the NC. While low-Fe bornite NCs (<7 atomic % Fe) were found to exhibit a strong LSPR peak in the NIR, similar to what has been observed previously in many copper sulfide NC systems,[42−44] an additional extinction feature centered at 490 nm, which is not typically observed in copper sulfide NCs, was also observed. For the high-Fe bornite compositions (above ∼9%), the small feature at 490 nm was found to have significantly increased intensity (Figure 1e), dominating the extinction characteristics of the material relative to the NIR LSPR response observed in the low-Fe bornite NCs.

Notably, absorption features with iron-content-dependent intensities have been observed in bulk-scale, Fe-doped, chalcopyrite-phase $CuGaS_2$ and $CuAlS_2$ materials.[45] These previous observations, along with the recent demonstration of quasi-static dielectric resonances in chalcopyrite-phase copper iron sulfide NCs,[10] led us to hypothesize that the strongly iron-content-dependent optical transition that we observe in bornite-phase copper iron sulfide may potentially be due to resonant transitions associated with a set of Fe-related states near the edge of the bornite VB. As a comparison, chalcopyrite-phase $CuFeS_2$ NCs with analogous sizes were also synthesized, with the extinction characteristics of bornite phase, 9.5 atomic % Fe NCs shown overlaid on the chalcopyrite $CuFeS_2$ extinction data (Figure 2). The previously reported DR is clearly observed in the chalcopyrite sample, at a similar frequency to that of the observed 490 nm extinction peak in the bornite NC samples. Furthermore, two additional distinguishable absorption features are observed as broad shoulders in the high-Fe bornite NCs, with peak positions at about 600 and 1250 nm, respectively (Figure 2). Notably, these two absorption bands also closely resemble the electronic transitions from the VB to the IB in chalcopyrite copper iron sulfide NCs (Figure 2) that were previously reported by Oguchi et al.,[46] suggesting the existence of two similar sub-band-gap transitions in the bornite-phase copper iron sulfide NCs.

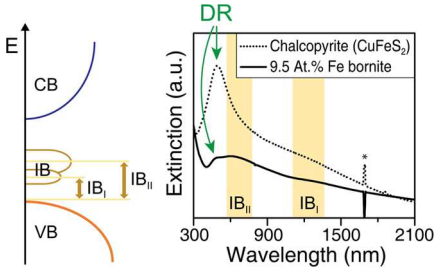

Figure 2. Schematic band structure of chalcopyrite-phase copper iron sulfide showing the optical transitions between states in the VB and the IB, and comparison of UV−vis−NIR extinction spectra of stoichiometric chalcopyrite NCs and bornite NCs with 9.5 atomic % Fe. Spectral artifacts caused by the NIR absorption bands of the chloroform solvent are marked by asterisks.

To test the hypothesis that the iron-related extinction feature of bornite in the visible region occurs due to the mid-gap Fe 3d states located above the VB edge, DFT calculations were carried out to determine the electronic structure of bornite-phase copper iron sulfide with different levels of iron content. Using intermediate-cubic-phase bornite (Cu_5FeS_4, $Fm3m$; 10 atomic % Fe) as a starting point, as corroborated by the experimental XRD patterns in Figure 1, the stoichiometry was systematically altered by gradually replacing tetrahedrally coordinated Cu atoms with additional Fe. The resulting DOS for three different stoichiometric bornite phases are shown in Figure 3. As can be seen from the atomic-projected DOS curves (Figure 3b), bornite indeed possesses an intense IB of states dominated by empty Fe 3d orbitals just above the VB. Moreover, the integrated DOS in the IB is strongly dependent on the iron content of the material (Figure 3c), agreeing with the iron-content-dependent intensity of the resonant optical transition observed at 490 nm in the bornite-phase NCs. Due to the strong similarities with the computational results of Gaspari et al.,[10] our data suggests that bornite NCs are an example of an IB semiconductor that exhibits a tunable, iron-content-dependent quasi-static DR in the visible-frequency range. Also, we observe that the partial substitution of Cu atoms in Cu_5FeS_4 by Fe not only increases the DOS of the IB but also decreases the gap between the VB and the IB, thus favoring the occurrence of a quasi-static DR by extending the range of negative permittivity.[10]

It is well known that nanoscale binary copper chalcogenides are prone to oxidation into more thermodynamically stable phases, and these phase changes are accompanied with changes in their optical characteristics.[47,48] Binary copper chalcogenides become self-doped upon exposure to air, through the well-established mechanism of Cu atom expulsion,[48] due to the high mobility of Cu ions in these lattices.[49] However, in a ternary Cu−Fe−S system like bornite or chalcopyrite, the iron atoms are in an energetically unfavorable tetrahedral coordination, which makes lattice expulsion of Fe atoms upon external influence more likely.[50] In fact, very few naturally occurring minerals are found with Fe atoms in tetrahedral coordination due to this reason,[51] and likewise, we found that oxidation of as-synthesized bornite NCs leads to the expulsion of Fe atoms from the lattice. The resulting variations in the iron content of the NCs have a large impact on their spectral characteristics. In case of the high-Fe bornite NCs, the initially dominant extinction feature at 490 nm decreases in intensity as the Fe atoms are slowly expelled from the NCs by exposing them to ambient conditions (Figure 4a), while the NIR LSPR feature gradually intensifies and eventually dominates the spectrum. The origin of this LSPR band in these oxidized NCs is similar to that of binary Cu−S NCs, where metal vacancies in the NC lattice leave holes behind as charge compensation. As Fe atoms are expelled from the

https://dx.doi.org/10.1021/acs.chemmater.0c04798
Chem. Mater. 2021, 33, 1821−1831

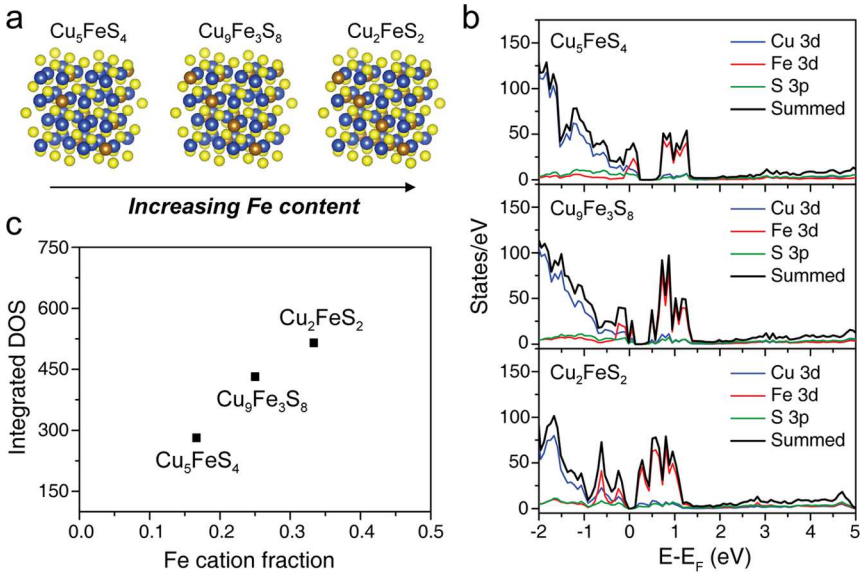

Figure 3. (a) Crystal structures, (b) atomic-projected DOS, and (c) integrated DOS of Fe 3d in the IB for a series of bornite copper iron sulfides.

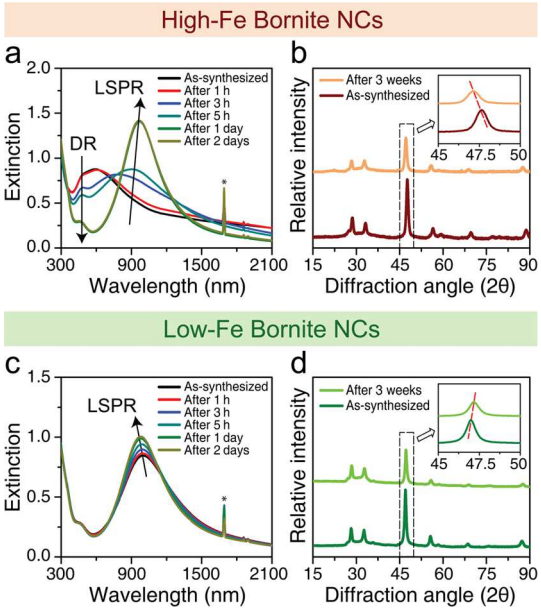

Figure 4. Optical and structural changes of the bornite NCs as a function of oxidation under ambient conditions. (a, b) high-Fe and (c, d) low-Fe bornite NCs. Panels a and c show the spectral evolution of the respective NCs as the oxidation progresses over the course of 2 days. Spectral artifacts caused by the NIR absorption bands of the chloroform solvent are marked by asterisks. Panels b and d include the XRD patterns collected for the as-synthesized NCs and the oxidized NCs after 3 weeks of air exposure.

lattice, the stoichiometry of these NCs approach that of a nanoscale Cu−S system and further oxidation leads to an LSPR response due to the increased density of holes in the VB. This behavior is more apparent in the extinction spectra of low-Fe bornite NCs (Figure 4c), which exhibit an LSPR band that gradually intensifies and blue-shifts upon air exposure. Such a blue shift could conceivably be explained by increased vacancy formation in bornite NCs upon oxidation, analogous to what is known to occur in binary copper chalcogenide NCs.[21,22,25] This will be discussed in more detail later in the text. XRD analysis of the NCs before and after these oxidative changes suggest that there was a slight shift to higher Bragg angles for all peaks in the XRD pattern of the low-Fe bornite sample upon exposure to air for 3 weeks (Figure 4d), indicating a decrease in the lattice parameter due to the formation of copper vacancies.[44,52] In contrast, it can clearly be seen that the lattice parameter of the high-Fe bornite NCs increases as the material is oxidized (Figure 4b). This increase in lattice parameter along with the decrease in intensity of the iron-related extinction feature indicates oxidatively driven expulsion of iron from the high-Fe bornite NCs.

The oxidation of the bornite NCs is also visually discernible, as the purple-colored dispersion of these NCs turns green upon air exposure (Figure 5a,b). The drastic differences in visual appearance between the DR-exhibiting, as-synthesized (Figure 5a) and LSPR-exhibiting, air-oxidized (Figure 5b) bornite NC samples are immediately apparent, while the sample stored in an inert-atmosphere glovebox shows very little change (Figure 5c) even after 45 days of storage. Likewise, the lattice parameter of the sample stored in the glovebox remains unchanged, while the lattice parameter of the sample stored in air increases significantly upon oxidation (Figure 5d). This clearly demonstrates that the particles are stable under inert atmosphere and that oxidizing conditions are necessary to drive the observed spectral evolution.

Further experiments to track the oxidative changes of the high-Fe bornite NCs were then carried out using elemental mapping *via* EDXS, leading to additional direct evidence that elucidates the role of iron in these systems, as discussed above. Figure 5e,f shows high-angle annular dark-field scanning TEM (HAADF-STEM) images for as-synthesized and oxidized bornite NCs, respectively. Apart from the readily discernible NCs in both images, some additional small granular matter is also immediately apparent in the oxidized NC sample (Figure 5f; arrows marking the regions of interest). EDXS mapping was then performed on a subset of the NCs in each sample (the analyzed regions are encircled by white lines in Figure 5e,f) to establish a spatial distribution of the constituent elements. The as-synthesized high-Fe bornite NCs exhibit Cu, Fe, and S evenly distributed throughout the individual NCs (Figure 5e). In contrast, while colocalization of the three elements over the NCs was still apparent after oxidation, significant leaching of

https://dx.doi.org/10.1021/acs.chemmater.0c04798
Chem. Mater. 2021, 33, 1821−1831

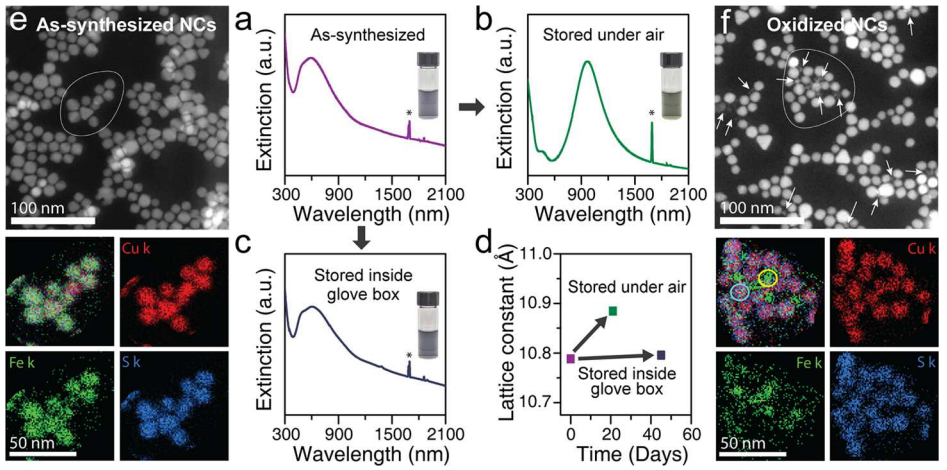

Figure 5. Oxidatively driven iron leaching and its influence on the optical signatures of bornite NCs. UV−vis−NIR extinction spectra of high-Fe bornite NCs: (a) as-synthesized, (b) after exposure to ambient air for 2 days, and (c) stored in a nitrogen-filled glovebox for 45 days. Spectral artifacts caused by the NIR absorption bands of the chloroform solvent are marked by asterisks. Photographs of the corresponding NC dispersions are included as insets, and the lattice constants of the NCs (as determined by XRD measurements) are included in panel (d). High-angle annular dark-field scanning transmission electron microscopy (HAADF-STEM) images and elemental mapping of the (e) as-synthesized and (f) oxidized high-Fe bornite NCs. The presence of iron-rich granular matter in the oxidized NC sample (panel f) is marked by arrows, while the white encircling lines in both panels demarcate the regions on which EDXS mapping was performed. The corresponding composite and individual elemental STEM-EDXS maps are included below each panel (e and f).

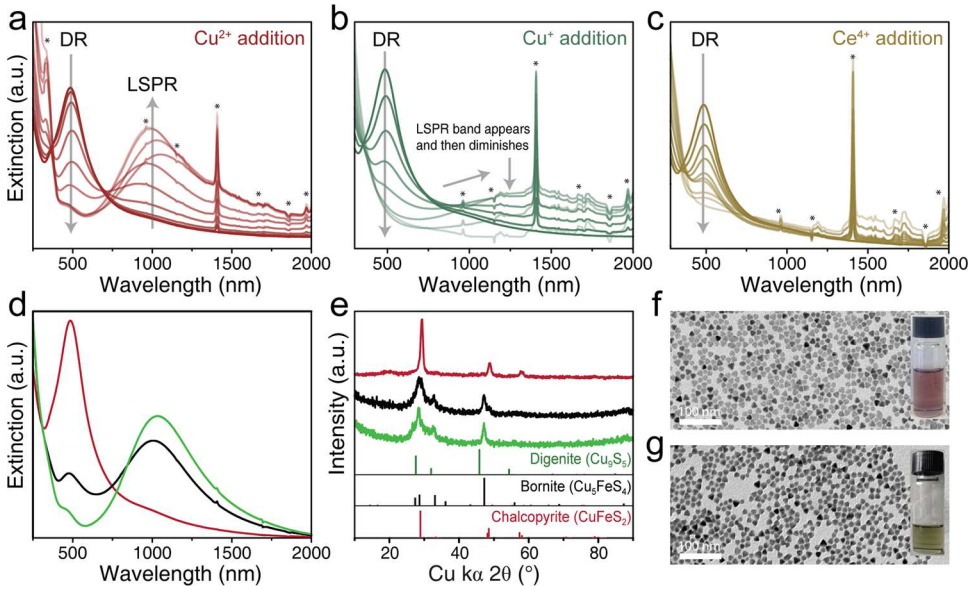

Figure 6. Evolution of the extinction spectra of chalcopyrite-phase $CuFeS_2$ NCs dispersed in chloroform during the stepwise addition of (a) Cu(II), (b) Cu(I), and (c) Ce(IV) solutions in methanol. Spectral artifacts caused by the absorption bands of the methanol solvent are marked by asterisks. (d) Extinction spectra and (e) XRD patterns of chalcopyrite NCs oxidized to different extents by Cu(II) ions. Red, black, and green curves correspond to the as-synthesized, partially oxidized, and fully oxidized samples, respectively. Database powder XRD patterns for chalcopyrite $CuFeS_2$ (PDF #00-037-0471; red lines), bornite Cu_5FeS_4 (PDF #98-000-6587; black lines), and digenite Cu_9S_5 (PDF #01-089-2072; green lines) are included for reference. Representative TEM images of (f) as-synthesized and (g) fully oxidized NCs, with the corresponding photographs of the NC dispersions included as insets.

iron from the NCs was clearly evident (Figure 5f). The iron signals in the EDXS maps were clearly more concentrated in the regions outside of the NCs after oxidation, revealing that the granular matter observed in the oxidized samples is predominantly composed of iron. These observations were further corroborated by elemental analysis using inductively coupled plasma optical emission spectroscopy (ICP-OES) of the as-synthesized and oxidized high-Fe bornite NCs. After the NCs were precipitated using an antisolvent, such that the precipitate and supernatant could be analyzed separately, larger concentrations of iron were detected in the supernatant of the oxidized sample (Table S4).

The above results demonstrate that the diminished intensity of the extinction feature at 490 nm can be attributed to the selective expulsion of iron atoms from the bornite NCs under oxidative stress, which leads to changes in the electronic structure and dielectric response of the material, thereby altering the optical extinction characteristics. The nature of this 490 nm extinction band was further probed by testing its dependence on the refractive index of the surrounding

https://dx.doi.org/10.1021/acs.chemmater.0c04798
Chem. Mater. 2021, 33, 1821−1831

medium. A systematic bathochromic shift of the extinction peak was observed with increasing solvent refractive index, providing additional evidence that this pronounced optical characteristic indeed arises from a Fe 3d IB-related quasi-static DR (Figure S11), as has been demonstrated in chalcopyrite $CuFeS_2$ NCs.[10] Computational calculations of the permittivity of the bornite phases verify that the real part of their permittivity indeed turns negative in the visible-frequency range as a consequence of their unique electronic structure (Figure S12), giving rise to a quasi-static DR in nanoscale particles (see Section S11 for calculation details).[10]

Further evidence for the generality of the role of Fe in the resonant extinction characteristics of ternary Cu−Fe−S NCs was also demonstrated by inducing similar spectral transformations in chalcopyrite-phase $CuFeS_2$ NCs. However, since chalcopyrite NCs are much less susceptible to ambient oxidation than the bornite phase, the use of more aggressive oxidizing agents or added ions was necessary to transform the spectral characteristics of the chalcopyrite NCs from an intense visible-frequency DR to an NIR LSPR. The colloidal chalcopyrite NCs used in these experiments were synthesized by a modified version of the procedure earlier reported by Ghosh et al.[5] NC purification and subsequent ion additions were performed in an inert atmosphere to eliminate the effects of air exposure. Solutions of Cu(II), Cu(I), and Ce(IV) ions in methanol were added to the chalcopyrite NC solutions in small increments in screw-capped cuvettes, and the associated spectral changes were recorded (Figure 6). The aforementioned transition from an intense DR to an LSPR is immediately apparent in Figure 6a, where the spectral changes associated with the progressive addition of Cu(II) ions are shown. Since Cu(II) ions are oxidizing in nature,[53] the intensity of the DR at 490 nm diminishes due to the oxidatively driven expulsion of Fe atoms once again, while the LSPR centered at 1000 nm subsequently increases in intensity due to the formation of cation vacancies in the material. On the other hand, when Cu(I) ions are added to chalcopyrite NCs (Figure 6b), the DR similarly loses intensity due to the expulsion of Fe atoms, but subsequently, the LSPR peak appears briefly and then shifts to longer wavelengths (lower energy), eventually disappearing as the addition of Cu(I) ions is continued. This difference in the evolution of the LSPR can be attributed to the replacement of holes in the NC lattice (left behind by the exiting Fe atoms) by the incoming copper atoms, when Cu(I) ions are added.[47,48] In the case of Cu(II) addition described before, the oxidizing nature of $CuCl_2$ takes precedence and gives rise to the vacancy-generated LSPR signature in the chalcopyrite NCs (Figure 6a). Similar spectral signatures are also recorded when Ce(IV) ions are added to the chalcopyrite NCs (Figure 6c), where the DR loses intensity as Ce(IV) ions are progressively added. However, in this case, the significantly stronger oxidizing nature of Ce(IV) affects the NCs adversely as their concentration in solution increases, eventually leading to complete dissolution of the NCs.

A deeper understanding of the DR in ternary Cu−Fe−S NCs was gained through analysis of the changes in the optical and structural properties of chalcopyrite NCs upon progressive addition of Cu(II) ions (Figure 6, panels d−f). The spectral responses for three samples at different stages of oxidation by Cu(II) ions are shown in Figure 6d. The as-synthesized (red curve) NCs exhibit the prominent DR at 490 nm, while the fully oxidized (green curve) NCs have a distinct LSPR signature, and the partially oxidized (black curve) NCs display spectral responses midway between these extreme cases, i.e., both DR and LSPR signatures are evident on the black curve. These NCs were further analyzed by way of XRD measurements (Figure 6e), and the diffraction pattern of the as-synthesized NCs matches with that of the bulk chalcopyrite powder XRD pattern. For the fully oxidized NCs, the diffraction pattern shows a mixture between the Fe-deficient bornite Cu−Fe−S phase (Cu_5FeS_4) and the Cu-deficient digenite Cu−S phase (Cu_9S_5). This occurrence of mixed phases in the oxidized NCs is not a surprise, since natural digenite always contains a small amount of iron and is considered to be stable only in the Cu−Fe−S system.[54] The Fe deficiency clearly indicates Fe expulsion from the NC lattice and was further corroborated using elemental analysis on the oxidized NCs. These NCs were washed (by adding an antisolvent like methanol), and the precipitate and supernatant were carefully collected for ICP-OES measurements. As demonstrated earlier for the bornite NCs (Figure 5), larger amounts of iron were detected in the supernatant, while the precipitate was found to be rich in copper and sulfur, confirming Fe expulsion from the NC lattice. The oxidation is also visually discernible, as the color of the NC dispersion changes from purple (Figure 6f) to green (Figure 6g) upon oxidation. This controlled oxidation does not affect the morphology of these NCs, as can be appreciated from the TEM images in Figure 6f,g, and hence size- and shape-related factors do not influence the observed spectral changes.

The occurrence of mixed phases (Cu−Fe−S and Cu−S) in the oxidized NCs clearly explains the observation of both DR and LSPR in these systems. In fact, this is the reason why the fully oxidized NCs still show some remnant DR signature at 490 nm for both bornite (Figure 5) and chalcopyrite NCs (Figure 6). One important distinction between the DR and LSPR signatures can be drawn from the oxidation experiments of the chalcopyrite NCs described above—while the intensity of both these spectral signatures were dependent on the level of oxidation, the position of the DR did not change during oxidative transformation, whereas the position of the LSPR did shift. This represents an important insight into the fundamental distinction between these two spectral processes—namely, that the DR in Cu−Fe−S NCs simply arises due to the unique band structure of the material and not due to vacancy doping, as is the norm in NCs of binary Cu−S phases. The LSPR signature in heavily doped semiconductor NCs, like that of vacancy-doped Cu−S NCs, is highly dependent on their charge carrier density.[55−57] Thus, both the position and intensity of the LSPR band are sensitive to oxidation and reduction of the NCs.[47,48,55−57] For instance, the oxidation of copper chalcogenide NCs is expected to result in a blue-shifted and intensified LSPR band due to the increase in the concentration of free charge carriers (holes) by the introduction of copper vacancies,[42,43,47,48] as is also evident in this case. However, the peak position of the DR at 490 nm in the $CuFeS_2$ NCs remains unchanged upon oxidation, even after transformation of the crystal structure from chalcopyrite to bornite, while its intensity is strongly suppressed. This result, which is not in accordance with other LSPR studies on copper chalcogenide NCs,[42−44,47] validates that the 490 nm extinction peak in chalcopyrite NCs is not attributable to collective oscillations of free charge carriers. It is rather a consequence of the quasi-static DR arising from an intermediate Fe d-band, and hence the intensity of this band decreases as Fe atoms are expelled from the NC lattice.

https://dx.doi.org/10.1021/acs.chemmater.0c04798
Chem. Mater. 2021, 33, 1821−1831

CONCLUSIONS

In summary, we have described a halide-assisted colloidal hot-injection synthesis of bornite NCs, which afforded both a monodisperse size distribution and compositional control, thus enabling comprehensive investigations into the influence of Fe content on the electronic structure and optical characteristics of ternary Cu−Fe−S nanomaterials. The Fe content in these bornite NCs was varied from 4.1 to 12.5%, giving rise to two fundamentally different types of resonant excitation, with a high Fe content inducing a strong quasi-static DR extinction band centered at 490 nm, and lower-Fe-content bornite NCs exhibiting a cation-vacancy-induced LSPR signature. Moreover, it was also demonstrated that DRs in these ternary copper iron sulfide NCs can be modulated through active manipulation of their Fe content *via* oxidative methods. The tunability of the optical responses from DR to LSPR *via* the oxidative removal of Fe from the NCs was investigated in detail, proving that the presence of Fe in these NCs is closely tied to the occurrence of the IB in their electronic structure that enables a Frölich resonance condition in the visible-frequency regime. These investigations entailed close monitoring of NC stoichiometry through elemental analysis and further confirmation by DFT calculations showing an associated increase in contribution to the DOS in the IB as the Fe content was increased, with HAADF-STEM elemental mapping and XRD measurements confirming that modulation of the optical response from a visible-frequency DR to a NIR LSPR can be attributed to the selective oxidation and expulsion of iron from the material. Interestingly, since both transitions occur in the visible-NIR region, they are visually discernible with the 490 nm (2.53 eV) DR inducing a purple color and the 1000 nm (1.24 eV) LSPR imparting a green color to the NC dispersion.

A similar set of transformations were observed when chalcopyrite NCs were subjected to the influence of oxidizing agents and added ions. While the as-synthesized chalcopyrite NCs exhibited the intense DR at 490 nm, strongly oxidizing conditions led to its evolution into a NIR LSPR, yielding further generality to the notion that the DR observed in nanoscale Cu−Fe−S systems is primarily due to the presence of the intermediate Fe d-band, and hence in turn, on the level of Fe incorporation in the material. The results presented here on these two Cu−Fe−S NC systems conclusively establish that the observed DR in these systems is indeed due to their unique band structure with the Fe IB positioned just above the VB edge, enabling a negative real permittivity in the visible region. Overall, this yields a deeper understanding of the optoelectronic characteristics of ternary copper iron sulfide NCs and demonstrates a pathway for optical modulation in these NCs, which in turn has ramifications for the development of material systems with a complex dynamic optical response.

EXPERIMENTAL SECTION

Materials. Copper(I) chloride (CuCl, 99.995%), Copper(II) chloride ($CuCl_2$, 97%), iron(III) chloride ($FeCl_3$, 97%), sodium chloride (NaCl, ≥99.0%), Tetrakis(acetonitrile)copper(I) hexafluorophosphate (TACF, $[Cu(CH_3CN)_4]PF_6$, 97%), trioctylphosphine oxide (TOPO, 90%), oleylamine (OAM, ≥98%), oleic acid (OA, 90%), 1-octadecene (ODE, 90%), cerium(IV) ammonium nitrate (CAN, $(NH_4)_2Ce(NO_3)_6$, ≥99.99%), and chloroform (anhydrous, ≥99%) were purchased from Sigma-Aldrich. Bis(trimethylsilyl)sulfide ($(S(Si(CH_3)_3)_2$, 95%) and ethanol (anhydrous, 200 proof, ≥99.5%) were obtained from Acros Organics. Methanol (Certified ACS) was purchased from Fisher Scientific. All chemicals were used as received without further purification.

Synthesis of Bornite NCs. All synthetic endeavors were carried out using standard Schlenk line techniques aided by a nitrogen-filled glovebox. In a typical synthesis, 0.8 mmol of copper(II) chloride (108 mg) and varying amounts of iron(III) chloride at a specified molar ratio (1:0.5, 1:0.75, 1:1, and 1:1.25) were mixed with different amounts of sodium chloride (between 0.6 and 1.8 mmol), 100 mg of TOPO, 1.2 mL of OAM, 1.2 mL of OA, and 5 mL of ODE in a three-neck round-bottom flask. The mixture was heated to 100 °C and degassed under vacuum for 1 h with vigorous stirring. Then, the flask was heated to 240 °C under a nitrogen atmosphere and maintained at this temperature for 1 h. Meanwhile, a sulfur precursor solution was prepared in a glovebox by diluting 275 μL of bis(trimethylsilyl)sulfide with 1.23 mL of ODE. Afterwards, 1.5 mL of the sulfur precursor solution was rapidly injected into the reaction flask containing the copper and iron precursors at 240 °C. The reaction temperature decreased to 225 °C after the injection. The reaction proceeded at this temperature for 90 s, and then the flask was removed from the heating mantle to decrease the temperature to 50 °C. To prevent solidification, 10 mL of anhydrous chloroform was added to the solution at 50 °C. The NCs were washed by the addition of 7.5 mL of ethanol, followed by centrifugation at 6000 rpm (4200 RCF) for 10 min. Finally, the NCs were dispersed in 5 mL of anhydrous chloroform and centrifuged at 1500 rpm (260 RCF) for 1 min to remove larger particles and byproducts.

Synthesis of Chalcopyrite NCs. This synthesis was performed using a modified version of the method previously reported by Ghosh et al.[5] In a three-neck round-bottom flask, 0.4 mmol of copper(I) chloride (40 mg) and 0.8 mmol of iron(III) chloride (130 mg) were mixed with 100 mg of TOPO, 1.2 mL of OAM, 1.2 mL of OA, and 5 mL of ODE. The reaction mixture was degassed at 100 °C for 1 h under vacuum with vigorous stirring. Thereafter, the reaction mixture was heated to 240 °C under a nitrogen atmosphere. At this temperature, 225 μL of bis(trimethylsilyl)sulfide in 1 mL of ODE were rapidly injected into the flask, and the mixture was allowed to react at 220 °C for 30 min. Subsequently, the flask was cooled to room temperature by removing the heating mantle, and then 10 mL of chloroform was added at 50 °C to prevent solidification of the reaction mixture. The final $CuFeS_2$ NCs were purified by adding 9 mL of ethanol, followed by centrifugation at 6000 rpm (4200 RCF) for 10 min. Finally, the resulting precipitate was dispersed in 5 mL of chloroform and centrifuged again at 1500 rpm (260 RCF) for 1 min to isolate any poorly stabilized NCs.

Chemical Modification of the Chalcopyrite $CuFeS_2$ NCs. These experiments involved the preparation of samples in a nitrogen-filled glovebox and then subsequent measurements of spectra in 3 mL screw-capped cuvettes. The NCs were carefully handled in this inert atmosphere to avoid any potential effects of air exposure (nb the postsynthesis NC purification steps and subsequent ion additions were all performed inside the glovebox). A typical experiment involved stepwise addition of oxidizing agents and ions directly to a cuvette containing 3 mL of $CuFeS_2$ NCs dispersed in chloroform, followed by measurement of extinction spectra after a 5 min wait time to let the reaction complete prior to the next addition. The oxidizing agents (CAN and $CuCl_2$) and ions (Cu(I) complex, TACF) were prepared at a 0.01 M concentration in methanol and added in 10 μL increments. Low-volume additions were used to minimize the antisolvent effect of methanol on the NC solutions and avoid the effects of aggregation on the recorded spectra.

Computational Details. DFT calculations were carried out using the Vienna ab initio simulation (VASP) package. Three different Cu−Fe−S materials of varying Fe concentration (Cu_2FeS_2, $Cu_9Fe_3S_8$, and Cu_5FeS_4) were modeled by taking a supercell approach composed of eight unit cells in a 2 × 2 × 2 expansion. The lattice constant of the cubic supercell was set as 10.95 Å.[58] Norm-conserving pseudopotentials[59,60] and unrestricted PBE + U[61,62] were used in VASP.[63−66] A cutoff energy of 500 eV was used for the plane-wave basis. The atomic positions were optimized while keeping the lattice constant fixed on a 2 × 2 × 2 Monkhorst-Pack k-point mesh of the Brillouin zone.[67] A 6

https://dx.doi.org/10.1021/acs.chemmater.0c04798
Chem. Mater. 2021, 33, 1821−1831

× 6 × 6 *k*-point mesh was used for a subsequent DOS calculation. Further details can be found in the Supporting Information.

Transmission Electron Microscopy (TEM) Analysis. Samples were prepared by dropping 15 μL of a dilute NC dispersion in chloroform on carbon-coated 200-mesh nickel TEM grids (Electron Microscopy Sciences). HRTEM, HAADF-STEM imaging, and EDXS analyses were performed at an accelerating voltage of 200 kV using an FEI Tecnai G2 F20 TEM equipped with an energy-dispersive X-ray spectroscopy detector (EDAX Element Silicon Drift Detector).

X-ray Diffraction (XRD) Analysis. Data collection was carried out using a Bruker D8 Discover diffractometer to determine the crystal structure of the materials. Samples were prepared by drop-casting concentrated NC dispersions onto a silicon substrate. XRD patterns were recorded using a Cu Kα X-ray source operating at 50 kV and 1000 μA.

Steady-State UV−vis−NIR Extinction Spectroscopy. Spectra of all NC dispersions were measured in a 1 cm path length quartz cuvette (Spectrocell) using either Varian Cary 60 UV−vis or Varian Cary 5000 UV−vis−NIR spectrophotometers.

Elemental Analysis. Concentrations of copper, iron, and sulfur were determined by ICP-OES using a Perkin Elmer Optima 8300. NCs were digested in aqua regia prepared from ultrapure nitric acid and hydrochloric acid in a 1:3 volume ratio. Once digestion was complete overnight, samples were diluted using (18.2 MΩ) deionized water. Calibrations were performed using multielement VII and sulfur ICP-OES standards obtained from EMD Millipore and Sigma-Aldrich, respectively.

■ ASSOCIATED CONTENT

Supporting Information

The Supporting Information is available free of charge at https://pubs.acs.org/doi/10.1021/acs.chemmater.0c04798.

Additional information on the effects of excess chloride addition on the synthesis of bornite NCs; TEM images and size distribution histogram; crystal structures of bornite and chalcopyrite phases; elemental composition analysis results; calculations of lattice parameters; HRTEM images of low-Fe and high-Fe bornite NCs and corresponding lattice parameter analysis; DFT calculations; UV−vis−NIR absorption spectra, XRD, and ICP-OES analysis data of bornite NCs upon oxidation; and analysis of the effect of changing the refractive index of the surrounding medium (PDF)

■ AUTHOR INFORMATION

Corresponding Author

Vincent C. Holmberg − *Department of Chemical Engineering, University of Washington, Seattle, Washington 98195-1750, United States; Molecular Engineering & Sciences Institute, University of Washington, Seattle, Washington 98195-1652, United States; Clean Energy Institute, University of Washington, Seattle, Washington 98195-1653, United States;* orcid.org/0000-0002-9591-8951; Email: holmvc@uw.edu

Authors

Soohyung Lee − *Department of Chemical Engineering, University of Washington, Seattle, Washington 98195-1750, United States;* orcid.org/0000-0001-6232-4420

Sandeep Ghosh − *Epi Process Technology, ASM America Inc., Phoenix, Arizona 85034-7200, United States;* orcid.org/0000-0002-1149-9199

Chad E. Hoyer − *Department of Chemistry, University of Washington, Seattle, Washington 98195-1700, United States;* orcid.org/0000-0003-2597-9502

Hongbin Liu − *Department of Chemistry, University of Washington, Seattle, Washington 98195-1700, United States;* orcid.org/0000-0001-9011-1182

Xiaosong Li − *Department of Chemistry and Molecular Engineering & Sciences Institute, University of Washington, Seattle, Washington 98195-1700, United States; Clean Energy Institute, University of Washington, Seattle, Washington 98195-1653, United States;* orcid.org/0000-0001-7341-6240

Complete contact information is available at: https://pubs.acs.org/10.1021/acs.chemmater.0c04798

Author Contributions

#S.L. and S.G. contributed equally to this work.

Notes

The authors declare no competing financial interest.

■ ACKNOWLEDGMENTS

S.L. and S.G. contributed equally to this work. S.L. performed the nanocrystal syntheses, experiments, and characterization. S.G. carried out the elemental mapping, provided the chalcopyrite data shown in Figure 6, and contributed to the general data analysis and organization. C.E.H., H.L., and X.L. performed the DFT calculations. S.L, S.G., and V.C.H. wrote the manuscript. S.G. and V.C.H. directed the research. S.G. and V.C.H. wish to acknowledge Matthew Panthani for helping them connect at the 2018 Gordon Research Conference (GRC) on Colloidal Semiconductor Nanocrystals, thereby enabling this work. This research was supported by the National Science Foundation (NSF) through the UW Molecular Engineering Materials Center, a Materials Research Science and Engineering Center (DMR-1719797). This material is based in part upon work supported by the University of Washington Molecular Engineering Institute, and part of this work was conducted at the Molecular Analysis Facility, a National Nanotechnology Coordinated Infrastructure site at the University of Washington which is supported in part by the National Science Foundation (grant ECC-1542101), the University of Washington, the Molecular Engineering & Sciences Institute, and the Clean Energy Institute.

■ REFERENCES

(1) Vaughan, D. J.; Craig, J. R. *Mineral Chemistry of Metal Sulfides*; Cambridge University Press, 1978; pp 72−155.

(2) Vaughan, D. J.; Tossell, J. A. Electronic structures of sulfide minerals - Theory and experiment. *Phys. Chem. Miner.* **1983**, *9*, 253−262.

(3) Ghosh, S.; Lu, H. C.; Cho, S. H.; Maruvada, T.; Price, M. C.; Milliron, D. J. Colloidal ReO_3 Nanocrystals: Extra Re d-Electron Instigating a Plasmonic Response. *J. Am. Chem. Soc.* **2019**, *141*, 16331−16343.

(4) Mantella, V.; Ninova, S.; Saris, S.; Loiudice, A.; Aschauer, U.; Buonsanti, R. Synthesis and Size-Dependent Optical Properties of Intermediate Band Gap Cu_3VS_4 Nanocrystals. *Chem. Mater.* **2019**, *31*, 532−540.

(5) Ghosh, S.; Avellini, T.; Petrelli, A.; Kriegel, I.; Gaspari, R.; Almeida, G.; Bertoni, G.; Cavalli, A.; Scotognella, F.; Pellegrino, T.; Manna, L. Colloidal $CuFeS_2$ Nanocrystals: Intermediate Fe d-Band Leads to High Photothermal Conversion Efficiency. *Chem. Mater.* **2016**, *28*, 4848−4858.

(6) Ferretti, A.; Rogers, D. B.; Goodenough, J. B. The relation of the electrical conductivity in single crystals of rhenium trioxide to the

conductivities of Sr_2MgReO_6 and Na_xWO_3. *J. Phys. Chem. Solids* **1965**, *26*, 2007−2011.
(7) Chen, P.; Qin, M.; Chen, H.; Yang, C.; Wang, Y.; Huang, F. Cr incorporation in $CuGaS_2$ chalcopyrite: A new intermediate-band photovoltaic material with wide-spectrum solar absorption. *Phys. Status Solidi A* **2013**, *210*, 1098−1102.
(8) Lucena, R.; Aguilera, I.; Palacios, P.; Wahno'n, P.; Conesa, J. C. Synthesis and Spectral Properties of Nanocrystalline V-Substituted In_2S_3, a Novel Material for More Efficient Use of Solar Radiation. *Chem. Mater.* **2008**, *20*, 5125−5127.
(9) Kehoe, A. B.; Scanlon, D. O.; Watson, G. W. The electronic structure of sulvanite structured semiconductors Cu_3MCh_4(M = V, Nb, Ta; Ch = S, Se, Te): prospects for optoelectronic applications. *J. Mater. Chem. C* **2015**, *3*, 12236−12244.
(10) Gaspari, R.; Della Valle, G.; Ghosh, S.; Kriegel, I.; Scotognella, F.; Cavalli, A.; Manna, L. Quasi-Static Resonances in the Visible Spectrum from All-Dielectric Intermediate Band Semiconductor Nanocrystals. *Nano Lett.* **2017**, *17*, 7691−7695.
(11) Avellini, T.; Soni, N.; Silvestri, N.; Fiorito, S.; De Donato, F.; De Mei, C.; Walther, M.; Cassani, M.; Ghosh, S.; Manna, L.; Stephan, H.; Pellegrino, T. Cation Exchange Protocols to Radiolabel Aqueous Stabilized ZnS, ZnSe, and $CuFeS_2$ Nanocrystals with ^{64}Cu for Dual Radio- and Photo-Thermal Therapy. *Adv. Funct. Mater.* **2020**, *30*, No. 2002362.
(12) Lv, X. S.; Deng, Z. H.; Miao, F. X.; Gu, G. X.; Sun, Y. L.; Zhang, Q. L.; Wan, S. M. Fundamental optical and electrical properties of nano-Cu_3VS_4 thin film. *Opt. Mater.* **2012**, *34*, 1451−1454.
(13) Liu, Y.; Ding, T.; Luo, X.; Li, Y.; Long, J.; Wu, K. Tuning Intermediate-Band Cu_3VS_4 Nanocrystals from Plasmonic-like to Excitonic via Shell-Coating. *Chem. Mater.* **2020**, *32*, 224−233.
(14) Vörös, M.; Galli, G.; Zimanyi, G. T. Colloidal Nanoparticles for Intermediate Band Solar Cells. *ACS Nano* **2015**, *9*, 6882−6890.
(15) Luque, A.; Martí, A.; Stanley, C. Understanding intermediate-band solar cells. *Nat. Photonics* **2012**, *6*, 146−152.
(16) Gabka, G.; Zybała, R.; Bujak, P.; Ostrowski, A.; Chmielewski, M.; Lisowski, W.; Sobczak, J. W.; Pron, A. Facile Gram-Scale Synthesis of the First n-Type $CuFeS_2$ Nanocrystals for Thermoelectric Applications. *Eur. J. Inorg. Chem.* **2017**, *2017*, 3150−3153.
(17) Vaure, L.; Liu, Y.; Cadavid, D.; Agnese, F.; Aldakov, D.; Pouget, S.; Cabot, A.; Reiss, P.; Chenevier, P. Doping and Surface Effects of $CuFeS_2$ Nanocrystals Used in Thermoelectric Nanocomposites. *ChemNanoMat* **2018**, *4*, 982−991.
(18) Jiang, X.; Zhang, S.; Ren, F.; Chen, L.; Zeng, J.; Zhu, M.; Cheng, Z.; Gao, M.; Li, Z. Ultrasmall Magnetic $CuFeSe_2$ Ternary Nanocrystals for Multimodal Imaging Guided Photothermal Therapy of Cancer. *ACS Nano* **2017**, *11*, 5633−5645.
(19) Li, B.; Yuan, F.; He, G.; Han, X.; Wang, X.; Qin, J.; Guo, Z. X.; Lu, X.; Wang, Q.; Parkin, I. P.; Wu, C. Ultrasmall $CuCo_2S_4$ Nanocrystals: All-in-One Theragnosis Nanoplatform with Magnetic Resonance/Near-Infrared Imaging for Efficiently Photothermal Therapy of Tumors. *Adv. Funct. Mater.* **2017**, *27*, No. 1606218.
(20) Girma, W. M.; Tzing, S. H.; Tseng, P. J.; Huang, C. C.; Ling, Y. C.; Chang, J. Y. Synthesis of Cisplatin(IV) Prodrug-Tethered $CuFeS_2$ Nanoparticles in Tumor-Targeted Chemotherapy and Photothermal Therapy. *ACS Appl. Mater. Interfaces* **2018**, *10*, 4590−4602.
(21) Comin, A.; Manna, L. New materials for tunable plasmonic colloidal nanocrystals. *Chem. Soc. Rev.* **2014**, *43*, 3957−3975.
(22) Liu, X.; Swihart, M. T. Heavily-doped colloidal semiconductor and metal oxide nanocrystals: an emerging new class of plasmonic nanomaterials. *Chem. Soc. Rev.* **2014**, *43*, 3908−3920.
(23) Park, J. Y.; Kim, S. J.; Chang, J. H.; Seo, H. K.; Lee, J. Y.; Yuk, J. M. Atomic visualization of a non-equilibrium sodiation pathway in copper sulfide. *Nat. Commun.* **2018**, *9*, No. 922.
(24) Li, B.; Wang, Q.; Zou, R.; Liu, X.; Xu, K.; Li, W.; Hu, J. $Cu_{7.2}S_4$ nanocrystals: a novel photothermal agent with a 56.7% photothermal conversion efficiency for photothermal therapy of cancer cells. *Nanoscale* **2014**, *6*, 3274−3282.
(25) Coughlan, C.; Ibáñez, M.; Dobrozhan, O.; Singh, A.; Cabot, A.; Ryan, K. M. Compound Copper Chalcogenide Nanocrystals. *Chem. Rev.* **2017**, *117*, 5865−6109.
(26) Akkerman, Q. A.; Genovese, A.; George, C.; Prato, M.; Moreels, I.; Casu, A.; Marras, S.; Curcio, A.; Scarpellini, A.; Pellegrino, T.; Manna, L.; Lesnyak, V. From Binary Cu_2S to Ternary Cu−In−S and Quaternary Cu−In−Zn−S Nanocrystals with Tunable Composition via Partial Cation Exchange. *ACS Nano* **2015**, *9*, 521−531.
(27) Lesnyak, V.; George, C.; Genovese, A.; Prato, M.; Casu, A.; Ayyappan, S.; Scarpellini, A.; Manna, L. Alloyed Copper Chalcogenide Nanoplatelets via Partial Cation Exchange Reactions. *ACS Nano* **2014**, *8*, 8407−8418.
(28) Wang, C.; Peng, L.; Yang, X.; Xie, R.; Feng, S. Cd-Cu-Fe-S quaternary nanocrystals exhibiting excellent optical/optoelectronic properties. *Nanoscale* **2019**, *11*, 6533−6537.
(29) Bhattacharyya, B.; Pandey, A. $CuFeS_2$ Quantum Dots and Highly Luminescent $CuFeS_2$ Based Core/Shell Structures: Synthesis, Tunability, and Photophysics. *J. Am. Chem. Soc.* **2016**, *138*, 10207−10213.
(30) Kowalik, P.; Bujak, P.; Penkala, M.; Kotwica, K.; Kmita, A.; Gajewska, M.; Ostrowski, A.; Pron, A. Synthesis of $CuFeS_{2-x}Se_x$—alloyed nanocrystals with localized surface plasmon resonance in the visible spectral range. *J. Mater. Chem. C* **2019**, *7*, 6246−6250.
(31) Ghosh, S.; Gaspari, R.; Bertoni, G.; Spadaro, M. C.; Prato, M.; Turner, S.; Cavalli, A.; Manna, L.; Brescia, R. Pyramid-Shaped Wurtzite CdSe Nanocrystals with Inverted Polarity. *ACS Nano* **2015**, *9*, 8537−8546.
(32) Zhong, H.; Lo, S. S.; Mirkovic, T.; Li, Y.; Ding, Y.; Li, Y.; Scholes, G. D. Noninjection Gram-Scale Synthesis of Monodisperse Pyramidal $CuInS_2$ Nanocrystals and Their Size-Dependent Properties. *ACS Nano* **2010**, *4*, 5253−5262.
(33) Ghosh, S.; Manna, L. The Many "Facets" of Halide Ions in the Chemistry of Colloidal Inorganic Nanocrystals. *Chem. Rev.* **2018**, *118*, 7804−7864.
(34) Reifsnyder, D. C.; Ye, X.; Gordon, T. R.; Song, C.; Murray, C. B. Three-Dimensional Self-Assembly of Chalcopyrite Copper Indium Diselenide Nanocrystals into Oriented Films. *ACS Nano* **2013**, *7*, 4307−4315.
(35) Wang, X.; Swihart, M. T. Controlling the Size, Shape, Phase, Band Gap, and Localized Surface Plasmon Resonance of $Cu_{2-x}S$ and Cu_xIn_yS Nanocrystals. *Chem. Mater.* **2015**, *27*, 1786−1791.
(36) Kim, S.; Kang, M.; Kim, S.; Heo, J.-H.; Noh, J. H.; Im, S. H.; Seok, S. I.; Kim, S.-W. Fabrication of $CuInTe_2$ and $CuInTe_{2-x}Se_x$ Ternary Gradient Quantum Dots and Their Application to Solar Cells. *ACS Nano* **2013**, *7*, 4756−4763.
(37) Bohren, C. F.; Huffman, D. R. *Absorption and Scattering of Light by Small Particles*; John Wiley & Sons, 1998; pp 130−157.
(38) Agrawal, A.; Cho, S. H.; Zandi, O.; Ghosh, S.; Johns, R. W.; Milliron, D. J. Localized Surface Plasmon Resonance in Semiconductor Nanocrystals. *Chem. Rev.* **2018**, *118*, 3121−3207.
(39) Link, S.; El-Sayed, M. A. Spectral Properties and Relaxation Dynamics of Surface Plasmon Electronic Oscillations in Gold and Silver Nanodots and Nanorods. *J. Phys. Chem. B* **1999**, *103*, 8410−8426.
(40) Philipp, H. R.; Ehrenreich, H. Optical Properties of Semiconductors. *Phys. Rev.* **1963**, *129*, 1550−1560.
(41) Marton, L. Experiments on Low-Energy Electron Scattering and Energy Losses. *Rev. Mod. Phys.* **1956**, *28*, 172−183.
(42) Jain, P. K.; Manthiram, K.; Engel, J. H.; White, S. L.; Faucheaux, J. A.; Alivisatos, A. P. Doped nanocrystals as plasmonic probes of redox chemistry. *Angew. Chem., Int. Ed.* **2013**, *52*, 13671−13675.
(43) Luther, J. M.; Jain, P. K.; Ewers, T.; Alivisatos, A. P. Localized surface plasmon resonances arising from free carriers in doped quantum dots. *Nat. Mater.* **2011**, *10*, 361−366.
(44) Kriegel, I.; Jiang, C.; Rodriguez-Fernandez, J.; Schaller, R. D.; Talapin, D. V.; da Como, E.; Feldmann, J. Tuning the excitonic and plasmonic properties of copper chalcogenide nanocrystals. *J. Am. Chem. Soc.* **2012**, *134*, 1583−1590.

https://dx.doi.org/10.1021/acs.chemmater.0c04798
Chem. Mater. 2021, 33, 1821−1831

(45) Teranishi, T.; Sato, K.; Kondo, K. Optical Properties of a Magnetic Semiconductor: Chalcopyrite $CuFeS_2$.: I. Absorption Spectra of $CuFeS_2$ and Fe-Doped $CuAlS_2$ and $CuGaS_2$. *J. Phys. Soc. Jpn.* **1974**, *36*, 1618−1624.
(46) Oguchi, T.; Sato, K.; Teranishi, T. Optical Reflectivity Spectrum of a $CuFeS_2$ Single Crystal. *J. Phys. Soc. Jpn.* **1980**, *48*, 123−128.
(47) Xie, Y.; Riedinger, A.; Prato, M.; Casu, A.; Genovese, A.; Guardia, P.; Sottini, S.; Sangregorio, C.; Miszta, K.; Ghosh, S.; Pellegrino, T.; Manna, L. Copper sulfide nanocrystals with tunable composition by reduction of covellite nanocrystals with Cu^+ ions. *J. Am. Chem. Soc.* **2013**, *135*, 17630−17637.
(48) Dorfs, D.; Hartling, T.; Miszta, K.; Bigall, N. C.; Kim, M. R.; Genovese, A.; Falqui, A.; Povia, M.; Manna, L. Reversible tunability of the near-infrared valence band plasmon resonance in $Cu_{2-x}Se$ nanocrystals. *J. Am. Chem. Soc.* **2011**, *133*, 11175−11180.
(49) Liu, H.; Shi, X.; Xu, F.; Zhang, L.; Zhang, W.; Chen, L.; Li, Q.; Uher, C.; Day, T.; Snyder, G. J. Copper ion liquid-like thermoelectrics. *Nat. Mater.* **2012**, *11*, 422−425.
(50) Silvester, E.; Grieser, F.; Healy, T. W.; Meisel, D.; Sullivan, J. C. Thermodynamics and kinetics of the reaction of copper(II) and iron(III) with ultra-small colloidal chalcopyrite ($CuFeS_2$). *J. Chem. Soc., Faraday Trans.* **1994**, *90*, 3301−3307.
(51) Kobayashi, H.; Onodera, H.; Kamimura, T. Electronic Properties of $CuFeS_2$ under Pressure Studied by Mössbauer Spectroscopy. In *Hyperfine Interactions (C)*; Springer: Dordrecht, 2002; pp 165−168.
(52) Riha, S. C.; Johnson, D. C.; Prieto, A. L. Cu_2Se nanoparticles with tunable electronic properties due to a controlled solid-state phase transition driven by copper oxidation and cationic conduction. *J. Am. Chem. Soc.* **2011**, *133*, 1383−1390.
(53) Miszta, K.; Brescia, R.; Prato, M.; Bertoni, G.; Marras, S.; Xie, Y.; Ghosh, S.; Kim, M. R.; Manna, L. Hollow and Concave Nanoparticles via Preferential Oxidation of the Core in Colloidal Core/Shell Nanocrystals. *J. Am. Chem. Soc.* **2014**, *136*, 9061−9069.
(54) Morimoto, N.; Koto, K. Phase relations of the Cu-S system at low temperatures: stability of anilite. *Am. Mineral.* **1970**, *55*, 106−117.
(55) Liu, L.; Zhong, H.; Bai, Z.; Zhang, T.; Fu, W.; Shi, L.; Xie, H.; Deng, L.; Zou, B. Controllable Transformation from Rhombohedral $Cu_{1.8}S$ Nanocrystals to Hexagonal CuS Clusters: Phase- and Composition-Dependent Plasmonic Properties. *Chem. Mater.* **2013**, *25*, 4828−4834.
(56) Faucheaux, J. A.; Stanton, A. L.; Jain, P. K. Plasmon Resonances of Semiconductor Nanocrystals: Physical Principles and New Opportunities. *J. Phys. Chem. Lett.* **2014**, *5*, 976−985.
(57) Kriegel, I.; Scotognella, F.; Manna, L. Plasmonic Doped Semiconductor Nanocrystals: Properties, Fabrication, Applications and Perspectives. *Phys. Rep.* **2017**, *674*, 674.
(58) Qiu, P.; Zhang, T.; Qiu, Y.; Shi, X.; Chen, L. Sulfide bornite thermoelectric material: a natural mineral with ultralow thermal conductivity. *Energy Environ. Sci.* **2014**, *7*, 4000−4006.
(59) Kresse, G.; Hafner, J. Norm-conserving and ultrasoft pseudopotentials for first-row and transition elements. *J. Phys.: Condens. Matter* **1994**, *6*, No. 8245.
(60) Vanderbilt, D. Soft self-consistent pseudopotentials in a generalized eigenvalue formalism. *Phys. Rev. B* **1990**, *41*, 7892−7895.
(61) Perdew, J. P.; Burke, K.; Ernzerhof, M. Generalized Gradient Approximation Made Simple. *Phys. Rev. Lett.* **1996**, *77*, No. 3865.
(62) Cococcioni, M.; de Gironcoli, S. Linear response approach to the calculation of the effective interaction parameters in the LDA +Umethod. *Phys. Rev. B* **2005**, *71*, No. 035105.
(63) Kresse, G.; Hafner, J. Ab initiomolecular dynamics for liquid metals. *Phys. Rev. B* **1993**, *47*, 558−561.
(64) Kresse, G.; Hafner, J. Ab initiomolecular-dynamics simulation of the liquid-metal−amorphous-semiconductor transition in germanium. *Phys. Rev. B* **1994**, *49*, 14251−14269.
(65) Kresse, G.; Furthmüller, J. Efficiency of ab-initio total energy calculations for metals and semiconductors using a plane-wave basis set. *Comput. Mater. Sci.* **1996**, *6*, 15−50.
(66) Kresse, G.; Furthmüller, J. Efficient iterative schemes for ab initio total-energy calculations using a plane-wave basis set. *Phys. Rev. B* **1996**, *54*, No. 11169.
(67) Monkhorst, H. J.; Pack, J. D. Special points for Brillouin-zone integrations. *Phys. Rev. B* **1976**, *13*, 5188−5192.

https://dx.doi.org/10.1021/acs.chemmater.0c04798
Chem. Mater. 2021, 33, 1821−1831